Synthesis and photocatalytic properties of nano iron oxide

Shabnam Shabanpour[1], *Mehran Riazian*[2] ✉

[1]*Department of Chemistry, Iran University of Science and Technology, Tehran, Iran*
[2]*Department of Engineering, Tonekabon Branch, Islamic Azad University, Tonekabon, Iran*
✉ *E-mail: m.riazian@toniau.ac.ir*

Published in Micro & Nano Letters; Received on 18th September 2017; Revised on 3rd November 2017; Accepted on 23rd November 2017

In this research, iron oxide nanostructure is prepared from $FeCl_3$ (iron chloride(III)) as a reactant by using the chemical co-precipitation method and calcined at 600°C. In this method, the chemical and physical characteristics drastically depend on the precursors, precipitants and preparation procedure. In this approach, 1,2,4,5-benzenetetracarboxylic acid, butanedioic acid, and hexanedioic acid are used as precipitants. The degradation rate of an organic pollutant dye (methylene blue) is investigated as a measure of photocatalytic activity. Nanostructure and photocatalytic activity are considered and studied by X-ray diffraction, scanning electron microscopy, energy dispersive X-ray spectroscopy, transmission electron microscopy, thermogravimetric analysis (TGA), Fourier transform infrared and ultraviolet–vis spectrophotometry. The effect of precipitants on the structure, lattice strain, nano crystallite growth and photocatalytic performance is studied. It is found that hexanedioic acid has an impressive effect on the nanostructure and photocatalytic performance, as a precipitant compared with pyromellitic acid and butanedioic acid.

1. Introduction: Elimination of organic pollutants specially dyes in loom industry wastewaters has been attractively investigated. The conventional methods could not remove the organic complex compounds such as organic toxic or infrangible chemical structures. The advanced oxidation processes have been effectively utilised to degrade the harmful organic complexes (aromatics, pesticides, and petroleum constituents) and turn them to small and safe molecules via highly reactive radicals ($\cdot OH^-$, $\cdot H^+$) [1]. The chemical properties and physical characteristics of photocatalysts such as structure, dimension, morphology, size and surface properties affect the photocatalytic activity [2]. The fabrication and preparation of iron oxide including α-Fe_2O_3, γ-Fe_2O_3 and Fe_3O_4 are subject to research due to their outstanding electrical, optical and magnetic properties [3]. Iron oxides are used as photocatalysts, gas sensors, drug delivery, high-density magnetic recording media, magnetic resonance imaging etc. [4–8]. Varied procedures and methods have been used to fabricate of iron oxide nanostructures such as thermal reactions, electrochemical, microemulsion, sol–gel, co-precipitation etc. [9, 10]. The co-precipitation method is versatile, cheap, high yields of products, decrease contamination and needs fewer solvents. The properties of products drastically depend on reaction condition (pH, time and temperature), reactants and precipitants. The chief targets of this research are to investigate the precipitants effect on α-Fe_2O_3 nanoparticles as well as, fabricate and investigate the photocatalytic performance of nano iron oxide by use of the co-precipitation method without using performed templates or catalysis to avoid any pollution. The photodegradation of methylene blue (MB) is verified in an aqueous solution under ultraviolet (UV) exposure.

2. Experimental procedure and details: In this Letter, $FeCl_3$ (iron(III) chloride, Merck ≥ 98%) is utilised as the precursor and for investigation of precipitance effect, ligands of carboxylic acids: 1,2,4,5-benzene tetracarboxylic acid (pyromellitic acid, Merck ≥ 99%, butanedioic acid (succinic acid, Merck ≥ 98%) and hexanedioic acid (adipic acid, Merck ≥ 98%) are used. The concentration and chemical properties of precursors and precipitants are summarised in Table 1. In the beginning, $FeCl_3$ and each of the carboxylic acids dissolved separately in the double distilled water. The pH of the aqueous solution of ligands is adjusted at 7 by adding dropwise the aqueous solution of NaOH (Merck ≥ 98%). Then, the aqueous solution of $FeCl_3$ is stirred for 30 min at 50°C and added gently to the precipitants' solution. Afterwards, the obtained solution is stirred for 30 min at 50°C. The brown concocted precipitate is filtered and rinsed three times with double distilled water and pure ethanol (Merck ≥ 99%), then centrifuged for 10 min at 3000 rpm. The precipitate is dried at 70°C. The obtained grained powder is calcined at 600°C with 10°C/min gradient, stayed for 3 h and cooled down with the same gradient.

The crystallite phases of the synthesised nanostructure are studied utilising X-ray diffraction (XRD) analysis (model: GBC-MMA), XRD patterns using K_α(Cu), 1.540 Å, 0.02° step size and 10°/min radiation speed. The scanning electron microscopy (model: Hitachi, S-4160) equipped with energy dispersive X-ray spectroscopy (EDX) is applied to take images of nanoparticles. The photodegradation of MB is performed under UV light (Philips, 253.7 nm) and determined using a Varian 50 scan. Transmission electron microscopy (TEM, Philips, CM120) is utilised to show the nanostructure of synthesised materials. The thermal treatment of the samples is investigated by TGA (model: Perkin Elmer, Paris). The chemical bonding is specified and recorded in KBr by Fourier transform infrared spectroscopy (FT-IR; model: Perkin-Elmer).

The photocatalyst degradation of MB is assigned as a measure to specify the photocatalytic activity of α-Fe_2O_3 nano powders. The photocatalytic activity experiments are carried out at room temperature (RT). The initial MB concentration is 100 mg/l. All experimental procedures to measure the photocatalytic activity are cited and presented in [11]. In all experiments, the temperature of the photoreactor is fixed at 27 ± 1°C by using a small ventilator. Reaction suspensions are prepared by adding 50 mg of α-Fe_2O_3nano powders that calcined at 600°C as a photocatalyst into 100 ml MB aqueous solution. As seen in Fig. 1, the absorbance peak is around 665 nm (λ_{max}).

3. Results and discussion: TGA technique is utilised in order to specify the removed organic component from the as-prepared sample and obtain the resultant product after calcination treatment. Fig. 2*a* shows triple steps of decomposition behaviour of the as-synthesised samples precipitated by hexanedioic acid and butanedioic acid. The TGA curve of sample 1 is the same as the sample 3 since their chain chemical structure is similar

doi: 10.1049/mnl.2017.0635

Table 1 Experimental conditions and concentration of precursor and precipitant

Sample	Concentration of $FeCl_3$	Precipitant	Concentration of precipitant
1	1 mmol (1.625 g)	hexanedioic acid	2 mmol (2.92 g)
2	3 mmol (0.54 g)	1,2,4,5-benzene tetracarboxylic acid	2 mmol (0.54 g)
3	1 mmol (1.625 g)	butanedioic acid	2 mmol (2.36 g)

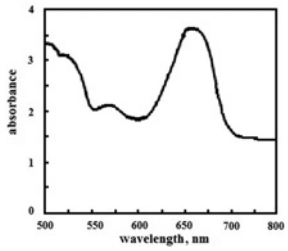

Fig. 1 *UV-visible absorbance spectra and absorbance peak at 660 nm*

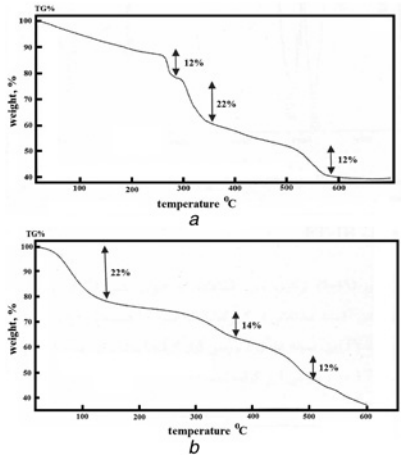

Fig. 2 *TGA curves of as-prepared samples that are synthesised by co-precipitation method*
a Samples 1 and 3
b Sample 2

compared with the cyclic chemical structure of sample 2. As seen in Fig. 2*a*, the first decomposition in the temperature range 283–290°C pertains to the evaporation of adsorbed-trapped water and the mass loss is about 12%. The second decomposition step in the temperature range 300–420°C is attributed to the decomposition of the organic compounds of as-synthesised samples and weight loss of this step is estimated about 22%. The third decomposition step in the temperature range 480–600°C corresponds to exit of the organic compounds of as-synthesised samples and the weight loss of this step is found to be 12%. The loss and burning of the residual organic compounds being completed at 600°C. Fig. 2*b* shows the triple steps of decomposition of the as-synthesised iron complex with pyromellitic acid (sample 2). The first decomposition in the temperature range 100–160°C pertains to the evaporation of adsorbed-trapped water and the mass loss is about 22%. The second decomposition stem in the temperature range 310–390°C is attributed to the elimination and evaporation of absorbed-trapped inter samples and weight loss of this step is estimated about 14%. The third decomposition step in the temperature range 480–600°C corresponds to the decomposition of the organic compounds of the as-synthesised samples and the weight loss of this step is found to be 12%. The loss and burning of the residual organic compounds is completed at 600°C. The calcination temperature of the as-synthesised samples determined at 600°C corresponds to this analysis.

XRD patterns of the samples calcined at 600°C are displayed in Fig. 3. The data of X-ray diffraction analysis are summarised in Table 2. The patterns correctly correspond and match to the hematite phase (α-Fe_2O_3, hexagonal, lattice constant $a = 5.035$ Å) ASTM (33-0664) card number. The absence of other crystalline phases or disturb peaks indicates the pure hematite crystallite phase. The average nanocrystallites size can be estimated using Scherrer's equation [12]

$$L = \frac{k\lambda}{2\beta\cos\theta}, \tag{1}$$

where $\lambda = 1.540$ Å is the X-ray radiation, β is the full-width at half maximum (FWHM) observed, θ is the Bragg diffraction angle (angle of X-ray incidence) and k known as the shape factor of grains is supposed to be 0.94. The calculated average nanocrystallite size of the iron oxide nanoparticles is found to be 78, 62 and 49 nm for samples 1, 2 and 3, respectively.

Lattice strains (ε) of nanocrystallites of iron oxides are obtained from the relation between FWHMs and sin θ on the observed diffraction peaks in 2θ ranging from 10° to 90° corresponding to Williamson–Hall's formula [13]

$$\beta\cos\theta = \frac{k\lambda}{L} + 4\varepsilon\sin\theta, \tag{2}$$

where β is the FWHM, L is the crystallite size, ε is the lattice strain, shape factor k is 0.94 to Scherrer's shape factor and $\lambda = 1.540$ Å.

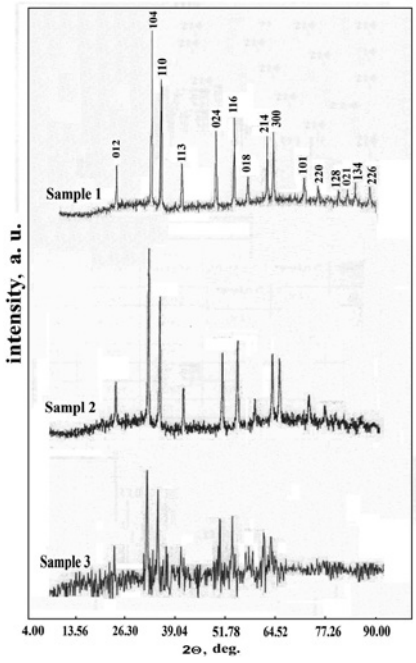

Fig. 3 *XRD patterns of α-Fe_2O_3 nanocrystallite samples with different precipitants*

Table 2 XRD characteristics: 2θ angle, d-space (d), grain size (r) of α-Fe_2O_3 nanocrystallites with different precipitants

Sample α-Fe_2O_3	$2\theta = 24.2°$ index miller: 012	$2\theta = 33.2°$ index miller: 104	$2\theta = 35.70°$ index miller: 110	$2\theta = 40.78°$ index miller: 113	$2\theta = 49.50°$ index miller: 024	$2\theta = 54.10°$ index miller: 116	$2\theta = 62.50°$ index miller: 214	$2\theta = 64.10°$ index miller: 300
	d space, Å							
1	3.68	2.70	2.51	2.20	1.84	1.69	1.48	1.45
2	3.67	2.70	2.51	2.20	1.84	1.69	1.48	1.45
3	3.69	2.70	2.52	2.21	1.84	1.69	1.48	1.45

Variation of $\beta \cos\theta$ against 4 $\sin\theta$ for different samples is near to be linear. ε is obtained from the slope of this linear dependence. Due to a low degree of crystallinity, there is no clear linearity between $\beta \cos\theta$ and 4 $\sin\theta$ [14]. The variation of $\beta \cos\theta$ against 4 $\sin\theta$ for diffraction peaks is shown in Fig. 4. In the sample ranging from room temperature (RT) to 600°C, the scattering of experimental data is high due to weakness and broadness of Bragg peaks, so that, it is not easy to calculate their FWHMs. Corresponding to Fig. 4, the lattice strain of sample 3 is maximum (0.368), sample 2 is (0.266) and sample 1 is minimum (0.173). This result indicates the effect of hexanedioic acid as a precipitant in sample 1 causes more arrangement, stability, and order in the crystallite structure and is in agreement with the XRD patterns. Moreover, it shows that the amorphous crystallite phase formed in sample 3 by the presence of butanedioic acid.

For investigation of chemical bonds in synthesised iron oxide nanoparticles, the infrared (IR) spectra are studied in the as-synthesised and calcined samples, while results indicate that the spectra of them are independent of the kind of precipitant (Fig. 5). The data of FTIR spectra of α-Fe_2O_3 nanoparticles are tabulated in Table 3. The band of the hydroxylic group (OH) of pure pyromellitic acid in the range 3400–3600 cm^{-1} is assigned to anti-symmetrical and symmetrical OH bonding stretching vibrational modes. This band shifts to 2800–3500 cm^{-1} for samples 1–3, which indicates carboxyl OH may not be ionised. This peak is broadened by disturbing with C–H stretching vibration of the kind of sp^2. The weak bands at 2854 and 2923 cm^{-1} are attributed to anti-symmetrical and symmetrical stretching vibrations of the methyl group, respectively. The anti-symmetrical stretching vibration band of C=O (carbonyl group) in pure pyromellitic acid appears within the wavenumbers range 1674–1713 cm^{-1}, while for samples 1–3 shifts to lower energy at 1558 cm^{-1}, due to the coordination of ligand to metal oxygen stretching vibrational modes [15]. The symmetrical stretching vibration of C=O in pure pyromellitic acid exists at 1371 cm^{-1} and appears at 1388 cm^{-1} for samples 1–3, whereas overlaps with the stretching band of C=C causes broadening of this peak. This difference in frequency probably indicates the single denticle of coordination. The stretching vibration of the C–O bond in pure pyromellitic acid is located in wavenumbers range 1210–1320 cm^{-1}, while appears at 1257 cm^{-1} for samples 1–3. The observed peak at 808 cm^{-1} belongs to the C–O bending

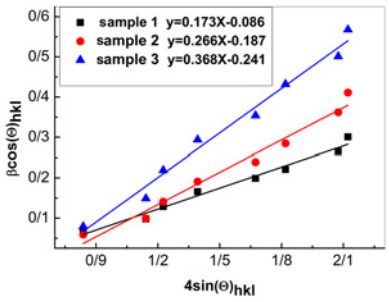

Fig. 4 *Variations of $\beta \cos\theta$ against 4 $\sin\theta$ of α-Fe_2O_3 nanocrystallite samples with different precipitants*

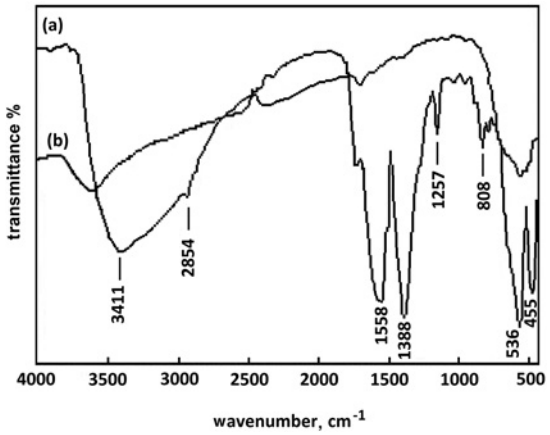

Fig. 5 *FT-IR spectra of iron oxide nanoparticles*
a Before calcinations at 600°C
b After calcinations at 600°C

vibration. After calcination, all the organic functional groups are removed and the strong double bands at 536 and 455 cm^{-1} belong to the Fe–O stretching vibration modes and reveal the accurate α-Fe_2O_3 crystalline phase [16].

TEM of the iron oxide nanostructure prepared from $FeCl_3$ and carboxylic acids by the co-precipitation method is shown in Fig. 6. This figure reveals the particles average size ~95, 81 and 54 nm for samples 1–3, respectively and this is close to the crystallite size calculated from Sherrer's equation.

The morphology of the samples synthesised by mentioned precipitants is revealed with the same magnifications. Fig. 7 shows the granular, congested and porous morphologies of samples 1 and 2, and, there are no individual particles. As seen, the particles in bee-shape are formed in integrated and compressed regions in sample 3(c). It is found that the morphology of sample 3 shows slightly interlaced and merged particles so that it is different from samples 1 and 2. Sample 3 has a smooth surface compared with samples 1 and 2. According to Fig. 7, from the average size distribution profiles, the particles' average size is estimated to be 87, 81 and 61 nm for samples 1–3, respectively. According to Fig. 7*a* for sample 1, shows particles consisting of aggregated particles as small as 20 nm in average size.

As seen in Fig. 8, the energy dispersive x-ray analysis (EDX) of the calcined samples 1, 2 and 3 reveals certainly the presence of Fe and O and therefore the formation of the pure α-Fe_2O_3 crystallite phase. This result is in agreement with the XRD conclusions.

The degradation rate of the aqueous solution of MB and α-Fe_2O_3 nanoparticles under UV irradiation is calculated as

$$\text{Photodegradation rate}\,\% = \ln\left[\frac{C_0 - C}{C}\right] \times 100, \tag{3}$$

$$\ln\left(\frac{C_0}{C}\right) = kt. \tag{4}$$

doi: 10.1049/mnl.2017.0635

Table 3 Data of FT-IR spectra of iron oxide nanoparticles per cm

Sample	Stretching vibration OH	Anti-symmetrical stretching C=O	Symmetrical stretching C=O	Symmetrical stretching	Bending C–O	Stretching Fe–O
pure pyromellitic acid	3600–3400	1750–1570	1370	1220–1310	790–620	—
1	3419–3120	1587, 1542	1421	1305	673	536, 465
2	3411–2854	1558	1388	1257	808	536, 455
3	3544–3000	1598	1442	1298	678	534, 459

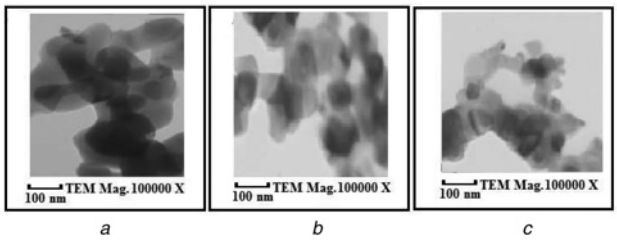

Fig. 6 *TEM images of nanoparticles calcined at 600°C*
a Sample 1
b Sample 2
c Sample 3

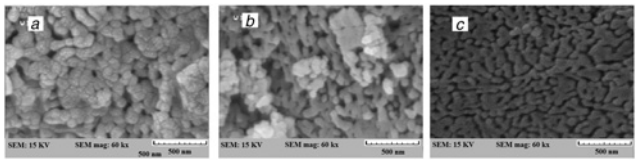

Fig. 7 *SEM images of nanoparticles calcined at 600°C*
a Sample 1
b Sample 2
c Sample 3

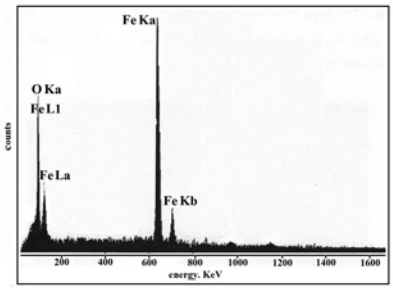

Fig. 8 *EDX spectra of the calcined samples prepared by co-precipitation method*

The relative concentration of methylene blue in the logarithmic scale $\ln(C_0/C)$ is traced against UV-Vis exposure time according to samples calcined at 600°C. The slope of the logarithmic plots is rate constant [17]. The photocatalytic measurements in Table 4 reveal the relevant kinetic variables, such as correlation coefficient (R^2) and the degradation rate constant (k). All reactions reveal linear relation, as shown in Fig. 9. As shown in Fig. 9, the rate constant, k, is deduced dependent on the presence of carboxylic precipitants. The rate constant (k) of sample 1 is the most valued compared with the samples 2 and 3 since more crystallinity of the α-Fe_2O_3 crystalline phase of sample 1 has an outstanding effect on degradation of the organic complex compounds. This increase could probably be due to the generation of the instant splitting of photo-induced electrons and holes and prolonging the recombination process of conduction and valence band carriers.

Table 4 Degradation data of the calcined samples prepared by co-precipitation method

Sample	k, min^{-1}	Correlation coefficient, R^2
1	0.060	0.99
2	0.045	0.98
3	0.027	0.98

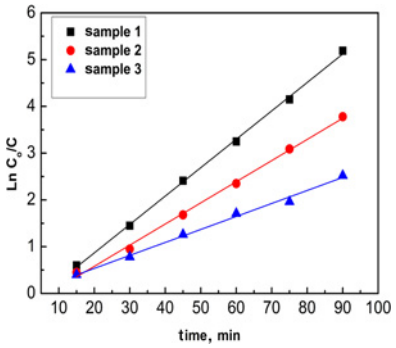

Fig. 9 *Exposure time dependence of ln(C_0/C) for the samples 1–3*

4. Conclusion: The nanostructure characterisation and photocatalytic performance of α-Fe_2O_3 nanoparticles are synthesised by the co-precipitation method and modified with carboxylic acids as precipitants (samples 1–3). XRD, scanning electron microscopy (SEM) and TEM analysis revealed that the average nano crystallite sizes in sample 1 are maximum compared with the other samples, where α-Fe_2O_3 nanocrystallites in the presence of hexanedioic acid show less lattice strain, more growth of nanocrystallites and a higher degree of crystallinity. SEM images of sample 3 show bee-like particles and smooth surface compared with the samples 1 and 2. It is found that the morphology of sample 3 shows slightly interlaced and merged particles so that it is different from samples 1 and 2. The XRD analysis shows the amorphous structure of sample 3. The photodegradation of MB is considered as a measure of photocatalytic activity. The experimental results show that the decomposition of a complex organic contaminant under UV illumination is a reliable technique to degrade completely MB. The obtained results show that sample 1 have higher photocatalytic activity compared with samples 2 and 3, therefore hexanedioic acid has an impressive effect on the α-Fe_2O_3 nanostructure and photocatalytic activity, as a precipitant compared with pyromellitic acid and butanedioic acid.

5. Acknowledgments: The authors appreciate Islamic Azad University, Tonekabon Branch for financial support through this research project.

6 References

[1] Karthik R., Kumar J.V., Chen S.M., *ET AL.*: 'A study of electrocatalytic and photocatalytic activity of cerium molybdate nanocubes decorated graphene oxide for the sensing and degradation of antibiotic drug chloramphenicol', *ASC Appl. Mater. Interfaces*, 2017, **9**, (7), pp. 6547–6559

[2] Qiong S., Xu Y.: 'Evaluating intrinsic photocatalytic activities of anatase and rutile TiO_2 for organic degradation in water', *J. Phys. Chem. C*, 2010, **114**, pp. 18911–18918

[3] Xu H., Wang X., Zhang L.: 'Selective preparation of nanorods and micro-octahedrons of Fe_2O_3 and their catalytic performances for thermal decomposition of ammonium perchlorate', *Powder Technol.*, 2008, **185**, pp. 176–180

[4] Nassar M.Y., Ahmed I.S., Mohamed T.Y., *ET AL.*: 'A controlled, template-free, and hydrothermal synthesis route to sphere-like [small alpha]-Fe_2O_3 nanostructures for textile dye removal', *RSC Adv.*, 2016, **6**, pp. 20001–20013

[5] Nassar M.Y., Ahmed I.S.: 'Template-free hydrothermal de-rived cobalt oxide nanopowders: synthesis, characterization, and removal of organic dyes', *Mater. Res. Bull.*, 2012, **47**, pp. 2638–2645

[6] Nassar M.Y.: 'Size-controlled synthesis of $CoCO_3$ and Co_3O_4 nanoparticles by free-surfactant hydrothermal method', *Mater. Lett.*, 2013, **94**, pp. 112–115

[7] Aly H.M., Moustafa M.E., Nassar M.Y., *ET AL.*: 'Synthesis and characterization of novel Cu(II) complexes with 3-substituted-4-amino-5-mercapto-1,2,4-triazole Schiff bases: a new route to CuO nanoparticles', *J. Mol. Struct.*, 2015, **1086**, pp. 223–231

[8] Behnajady M.A., Taba H., Modirshahla N., *ET AL.*: 'Photocatalytic activity of Cu doped TiO_2 nanoparticles and comparison of two main doping procedures', *Micro Nano Lett.*, 2013, **8**, (7), pp. 345–348

[9] Mishima F., Takeda S., Izumi Y., *ET AL.*: 'Three dimensional motion control system of ferromagnetic particles for magnetically targeted drug delivery systems', *IEEE Trans. Appl. Supercond.*, 2016, **16**, pp. 1539–1542

[10] Zhong J., Ch Cao.: 'Nearly monodisperse hollow Fe_2O_3 nanoovals: synthesis, magnetic property and applications in photocatalysis and gas', *Sens. Actuators B*, 2010, **145**, pp. 651–656

[11] Riazian M.: 'Dependence of photocatalytic activity of TiO_2–SiO_2 nanopowders', *J. Nano Struct.*, 2014, **4**, pp. 433–441

[12] Riazian M.: 'Nanostructural characterization and lattice strain of TiO_2–Al_2O_3–SiO_2 coating on glass and Si(100) substrates', *J. Chil. Chem. Soc.*, 2016, **61**, pp. 2870–2877

[13] Zaka A.K. Abd, Majida W.H., Abrishamib M.E., *ET AL.*: 'X-ray analysis of ZnO nanoparticles by Williamson–Hall and size-strain plot methods', *Solid State Sci.*, 2011, **13**, pp. 251–256

[14] Inagaki M., Nonaka R., Tryba B., *ET AL.*: 'Dependence of photocatalytic activity of anatase powders on their crystallinity', *Chemosphere*, 2006, **64**, pp. 437–445

[15] Hosseinian A., Rezaei H., Mahjoub A.R.: 'Preparation of nanosized iron oxide and their photocatalytic properties for Congo red', *World Academy Sci. Eng. Tech.*, 2011, **52**, pp. 736–739

[16] Nakamato K.: 'Infrared and Raman spectra of inorganic and coordination compounds' (John Wiley & Sons, New Jersey, 2014, 6th edn.)

[17] Si L.L., Huang Z.A., Lv K.L., *ET AL.*: 'Facile preparation of Ti^{3+} self-doped TiO_2 nanosheets with dominant {0 0 1} facets using zinc powder as reductant', *J. Alloys Compd.*, 2014, **601**, pp. 88–93

doi: 10.1049/mnl.2017.0635